J. Fluid Mech. (1990), vol. 214, pp. 579–597
Printed in Great Britain

Nonlinear dynamics of vertical vorticity in low-Prandtl-number thermal convection

By JOSEP M. MASSAGUER, ISABEL MERCADER AND MARTA NET

Departament de Fisica Aplicada, Jorge Girona Salgado s/n, Universitat Politecnica de Catalunya, Barcelona 08034, Spain

(Received 3 January 1989 and in revised form 27 October 1989)

The aim of the paper is to examine the nonlinear dynamics of a truncated system modelling low-Prandtl-number thermal convection. The model describes situations where the primary flow is not a straight roll and the dynamics is dominated by the production of axial flow along the axis of bent rolls or of swirl along ring vortices. The physical mechanism for these processes is a spontaneous growth (i.e. bifurcation) of a vertical vorticity mode, breaking the two-dimensional symmetry of the system. A description of the model can be found in Massaguer & Mercader (1988) where the physics and the numerical results have been checked against laboratory experiments. The nonlinear dynamics of that model will be discussed in the more academic case of free boundaries, as it has been shown that for sufficiently small Prandtl numbers straight rolls cannot be expected to be the primary flow near the onset of convection (Busse & Bolton 1984). Two clearly differentiated time-dependent regimes have been found and they correspond to small and intermediate Péclet numbers. In the former regime there exists a transition to chaos with the whole scenario being dependent on a symmetry invariance common to a large number of confined flows. The route to chaos is made up of a sequence of homoclinic explosions giving rise to a cascade of period doublings, with the whole scenario being different from that of a Feigenbaum's cascade.

1. Introduction

Thermal convection in low-Prandtl-number fluids, such as liquid metals or astrophysical plasmas, is still a poorly understood phenomenon. Difficulties involved in conducting clean and controlled laboratory experiments together with requirements of high resolution for numerical simulations make progress very slow, in spite of the relevance of the subject. We have chosen to view these flows as being almost inviscid, with their dynamics being dominated by shear-type instabilities and we have concentrated on the growth and subsequent dynamics of a vertical vorticity component as being the most relevant process.

The purpose of the present paper is to examine thermal convection for Prandtl numbers σ small enough to display some signature of the limit $\sigma \ll 1$. There are in fact two such limits. The first one is a regular limit and we shall call it the zero-Prandtl-number limit for obvious reasons, though its existence is bounded to mild supercritical regimes. The second limit seems to be a singular one. Besides their academic interest, the existence of such limits and the knowledge of their dynamics is a major question in astrophysical fluid dynamics where fluids are almost inviscid and largely conducting.

As discussed elsewhere (Massaguer & Mercader 1984, 1988) vertical vorticity can be produced in several contexts. First, in finite containers, where the existence of a non-zero vertical vorticity component can be a requirement to fulfil boundary conditions. Secondly, in flows not displaying two-dimensional geometry, as in such cases the growth of a non-zero vertical vorticity component is a dynamic requirement from the Navier–Stokes equation, though often of little relevance. In some cases that component can even be artificially killed without any dramatic change in the dynamics, as shown, for instance, by the so-called amplitude equations (Newell & Whitehead 1969). The reason is that in this context the vertical vorticity component is a slave mode, in the sense that it is a damped mode externally forced by the main field (see Haken 1983 for a discussion on slave modes). As mentioned before, its feedback can often be neglected, so vertical vorticity does not play any role. The best known exception comes from the oscillatory instability, where short-cutting the feedback kills the instability (Zippelius & Siggia 1982; Siggia & Zippelius 1983).

Elsewhere we have called such instabilities shape instabilities, for they are geometrical requirements of the main field. To be precise, in these instabilities the growth of vertical vorticity does not break the symmetry of the system, yet the symmetry must be broken before it can grow (the source term is a Jacobian and is zero for any two-dimensional flow). There still exists an additional source of instability for the vertical vorticity. It is a shear instability, which we have called instability of swirl as it grows as an azimuthal component in toroidal flows, with the result that it fundamentally breaks the symmetry of the primary flow.

The instability of swirl is an instability that cannot be triggered unless the primary flow is a bent roll or a torus, as could be the case for convection in small-aspect-ratio boxes. It is an instability well known in vorticity dynamics where it appears in bent filaments as an axial flow or in ring vortices as a swirl. The agreement of some results in Massaguer & Mercader (1988, hereafter called Paper I) with experiments in large-aspect-ratio boxes suggests that such an instability might be active also if conveniently coupled with the oscillatory instability, where the rolls are bent dynamically by a wavy motion like a vibrating string, before the instability of swirl could be triggered. That instability must be particularly active in the case of free boundary conditions where no stable, steady convection flow is possible near the onset of convection (Busse & Bolton 1984; Bolton & Busse 1985).

To the best of our knowledge, the first indication of a spontaneous growth of a permanent vertical vorticity component was reported by Graham (1977) in a pioneering work on three-dimensional numerical simulation of thermal convection in a compressible fluid. He found a time-dependent, but persistent, component that can hardly be associated with any shape instability. The relevance of such a result has been magnified by the very recent discovery of persistent spots of vertical vorticity in the solar photosphere (Brandt *et al.* 1988; Toomre 1988), which might be taken as an indication of high activity in terms of vertical vorticity dynamics deep in the convection zone.

To describe the flow the same model is used as in Paper I, though now we concentrate on the case of free boundaries. The model is a highly truncated modal expansion in which, in order to deal with shear-type instabilities, a vertical vorticity component is still present. The model was shown to be quite reasonable for modelling thermal convection in mercury, $\sigma = 0.025$, at mildly supercritical values as computed frequencies and fluxes were well within the range of the experimental measurements. Obviously, this is not a good enough basis for trusting its detailed dynamics, but it

does provide a basis for some confidence in the relevant balances and scalings, even for the time-dependent problem.

Most of the scenario to be shown is induced by the skew-symmetry of the velocity and temperature fields about the midplane

$$\{v_x, v_y, v_z, T\} \to \{v_x, v_y, -v_z, -T\},$$
$$\{x, y, z\} \to \{x+x_0, y+y_0, -z\},$$

with the origins for the temperature T and the z-coordinate taken in the middle of the convection layer. As usual $\boldsymbol{v}$ is the velocity field, and $\{x_0, y_0\}$ are constant space shifts. That symmetry is a rather general property fulfilled for most flows confined in finite ($x_0 = y_0 = 0$) or periodic boxes (see, for instance, Knobloch *et al.* 1986). In that respect the reader must be aware that for planar flows x_0 and y_0 have to be different from zero in order to prevent that symmetry from becoming an identity, but that is not the case for other flows, in particular for three-dimensional ones. Therefore, the scenario to be described can exist even for finite containers.

There is also a second symmetry invariance of a very general nature. It is a reversal in vertical vorticity that we can write as

$$\{v_x, v_y, v_z, T\} \to \{v_x, -v_y, v_z, T\},$$
$$\{x, y, z\} \to \{x+x_0, -y-y_0, z\},$$

with both x- and y-coordinates being exchangeable. That symmetry is still present in our truncated model but we have not found any particular scenario related to that symmetry in the range of variables explored.

A system invariant against symmetries, say invariant against a finite symmetry group to be precise, can be suspected to be a candidate to display global instabilities. If it is invariant against a finite symmetry group every asymmetric solution is replicated as many times as there are elements in the group. If these asymmetric solutions are time dependent and their basins of attraction come close enough, we can expect reconnections, mergings and, working backwards, splittings. There are at least two well-known examples of transition to chaos in fluids where such symmetry invariances play an important role: the Lorenz model (Sparrow 1982; Guckenheimer & Holmes 1983) and thermohaline convection (Knobloch *et al.* 1986). The existence of one such scenario for the Ginzburg–Landau equation is also worth mentioning (Kuramoto & Koga 1982) because of its profound relationship to fluid dynamic problems.

The number of known routes to chaos is very limited and most of them concern sequences of local instabilities in periodic solutions (Eckmann 1981). They are, certainly, easier to classify than global instabilities, for they simply concern the evolution of a few eigenvalues in parameter space, not the whole topological structure of the vector field. Nevertheless, global instabilities are as physical as local instabilities, at least in finite containers where finite symmetries are usually present. So, any realistic physical model displaying global instabilities is welcome.

The present paper concentrates, mostly, on the dynamics of the nonlinear, time-dependent model described in Paper I. In §2 we review the main properties of the model. The structure and stability of the steady solutions is discussed in §3, where a zero-Prandtl-number model is presented, and the time dependence is examined in §4. Finally, in §5 we advance some conclusions concerning the physical and mathematical relevance of the model.

2. Description of the mathematical model

The present paper concerns low-Prandtl-number thermal convection in a plane-parallel domain, horizontally periodic, bounded by two horizontal plates and filled with a Boussinesq fluid. The model used has been extensively described in Paper I and only a brief summary of it will be provided here. The velocity field is expressed in terms of two scalar potentials associated with the vertical components of the velocity v_z and vorticity ω_z. Both of them, together with the temperature T, are the whole set of variables needed to describe the problem. In the present model we assume for these variables the following shape assumption:

$$\left.\begin{aligned} v_z &= f(x,y)\, W(z,t), \\ \omega_z &= f(x,y)\, \xi(z,t), \\ T &= \bar{T}(z,t) + f(x,y)\, \theta(z,t), \end{aligned}\right\} \tag{2.1}$$

where $f(x,y)$ is an eigenfunction of the horizontal Laplacian operator $\nabla_1^2 f = -a^2 f$ with zero horizontal average. The horizontal components of the velocity field can be written as

$$v_x = a^{-2}(\partial_x f \partial_z W + \partial_y f \xi),$$

$$v_y = a^{-2}(\partial_y f \partial_z W - \partial_x f \xi).$$

With such an expansion, the Navier–Stokes and the heat equations take the form

$$(\sigma^{-1}\partial_t - \nabla^2)\nabla^2 W = -R a^2 \theta - C\sigma^{-1}(W \partial_z \nabla^2 W + 2\,\partial_z W \nabla^2 W + 3\xi \partial_z \xi), \tag{2.2a}$$

$$(\sigma^{-1}\partial_t - \nabla^2)\xi = -C\sigma^{-1}(W \partial_z \xi - \xi \partial_z W), \tag{2.2b}$$

$$(\partial_t - \nabla^2)\theta = -W \partial_z \bar{T} - C(2W \partial_z \theta + \theta \partial_z W), \tag{2.2c}$$

$$(\partial_t - \partial_{zz}^2)\bar{T} = -\partial_z (W\theta), \tag{2.2d}$$

where $\nabla^2 = \partial_{zz}^2 - a^2$, R is the Rayleigh number, σ is the Prandtl number and C is a constant associated with the planform $f(x,y)$. The computations have been carried out with $C = 1/\sqrt{6}$. Also, unless otherwise stated, it will be assumed that $a = 2.22$, which corresponds to the critical value for the linear problem. At the boundaries the so-called free boundary conditions will be assumed for velocity: zero vertical velocity and no tangential stresses, and for the temperature perfectly conducting plates:

$$W = \partial_{zz}^2 W = \partial_z \xi = \theta = 0 \quad (z = \pm \tfrac{1}{2}), \tag{2.3a}$$

$$\bar{T} = \mp \tfrac{1}{2} \quad (z = \pm \tfrac{1}{2}). \tag{2.3b}$$

The Nusselt number, defined as

$$N = -\partial_z \bar{T} + W\theta, \tag{2.4}$$

will be evaluated at the top boundary, whenever not constant, and the Reynolds number

$$Re = CW/\sigma \tag{2.5}$$

will be evaluated in the centre of the layer. As a measure of the departure from pure poloidal flow we shall introduce the helicity, defined as $h = \boldsymbol{\omega} \cdot \boldsymbol{v}$, its horizontally averaged value being provided by the expression

$$\bar{h} = 2\xi W + a^{-2}(\partial_z \xi \partial_z W - \xi \partial_{zz}^2 W), \tag{2.6}$$

where $\bar{h}$ is obviously zero in the absence of vertical vorticity.

3. Structure and stability of the steady solutions

The system (2.2) has two different families of steady solutions, as can be seen from figure 1, where the Nusselt number versus the Rayleigh number for every computed solution and for a Prandtl number $\sigma = 0.025$ has been plotted. The first family, defined by the condition $\xi = 0$, has been plotted as a dot-dashed line. It exists for the whole range of parameters, whereas a second family of steady solutions, a dashed line, defined by the condition $\xi \neq 0$, branches at a supercritical Rayleigh number $R_T = 723$.

Finally, the $\xi \neq 0$ family of solutions becomes unstable through a Hopf bifurcation at a Rayleigh number $R_t = 882$, plotted as an open circle. In figure 1 we have also included as asterisks, the averaged Nusselt numbers for every time-dependent solution computed. As for the rigid boundary case (see Paper I), the second family of steady solutions is highly inefficient for transporting heat, the only difference between the free and rigid boundary case being that in the former the bifurcation is supercritical throughout the explored range, $\sigma = 10^{-4}$–10, while in the latter it is subcritical. That range of parameters also includes a chaotic region, indicated as a thick line on the Rayleigh-number axis.

3.1. *On the zero-Prandtl-number limit*

A remarkable property of system (2.2) and (2.3) is the presence of an asymptotic limit for small σ-values. In figure 2 the Rayleigh numbers R_T and R_t introduced above, together with the frequency ω for the Hopf bifurcation, scaled as ω/σ (i.e. measured in terms of the viscous timescale), have been plotted as a function of σ. Each of these values shows an asymptotic limit for $\sigma \ll 1$, with $R_T = 720$, $R_t = 874.5$ and $\omega/\sigma = 7.02$ being their asymptotic values. A similar behaviour, not displayed in the figure, can be observed for the amplitudes of the velocity field at the bifurcation points as measured by its Reynolds numbers.

To explain the existence of such a small σ-limit we must rescale the variables in (2.2) as $\partial_\tau = \sigma^{-1}\partial_t$, $\tilde{W} = CW/\sigma$, $\tilde{\xi} = C\xi/\sigma$, and $\tilde{\theta} = C\theta/\sigma$. With that definition τ is the viscous timescale and $\tilde{W}(z,\tau)$ is the local Reynolds number (please note the C-factor, not included in Paper I). At leading order in σ, for $\sigma \ll 1$, (2.2) becomes

$$(\partial_\tau - \nabla^2)\nabla^2\tilde{W} = -Ra^2\tilde{\theta} - (\tilde{W}\partial_z\nabla^2\tilde{W} + 2\partial_z\tilde{W}\nabla^2\tilde{W} + 3\tilde{\xi}\partial_z\tilde{\xi}), \tag{3.1a}$$

$$(\partial_\tau - \nabla^2)\tilde{\xi} = -(\tilde{W}\partial_z\tilde{\xi} - \tilde{\xi}\partial_z\tilde{W}), \tag{3.1b}$$

$$0 = \tilde{W} + \nabla^2\tilde{\theta}, \tag{3.1c}$$

where (2.2d) has been integrated to $\partial_z\bar{T} = -1$.

System (3.1) approximates (2.2) only up to $\tilde{W}$, $\tilde{\xi}$, $\tilde{\theta}$ and ∂_τ of order one. So we can term that system a low-Reynolds-number flow, or the slow limit or, even better, the small-Péclet-number limit, with the Péclet number defined as $Pe = \sigma Re$ (i.e. $Pe = CW$), usually taken to be a measure of the fraction of advected heat in the total flux. In fact, to leading order we have $N - 1 \approx 0$. That limit had been examined by Gough, Spiegel & Toomre (1975) for the time-independent case and was identified in their paper as the $R\sigma \ll 1$ limit, with $N - 1 \approx O(R^2\sigma^2)$, in agreement with our approximation – see §4.1. System (3.1) has been integrated in order to show its range of validity and the results will be displayed below, but we can anticipate that it is a good approximation of (2.2) for a range of values of R.

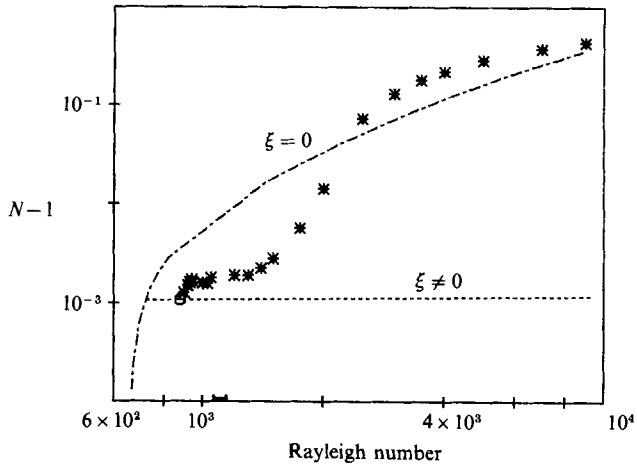

FIGURE 1. Nusselt number–versus Rayleigh number for $\sigma = 0.025$ and $a = 2.22$. Dashed and dot-dashed lines correspond to $\xi \neq 0$ and $\xi = 0$ steady solutions, respectively. Periodic solutions are denoted by an asterisk (*). A thick line in the Rayleigh-number axis delimites the range $1070 < R < 1140$ where we have found chaotic solutions.

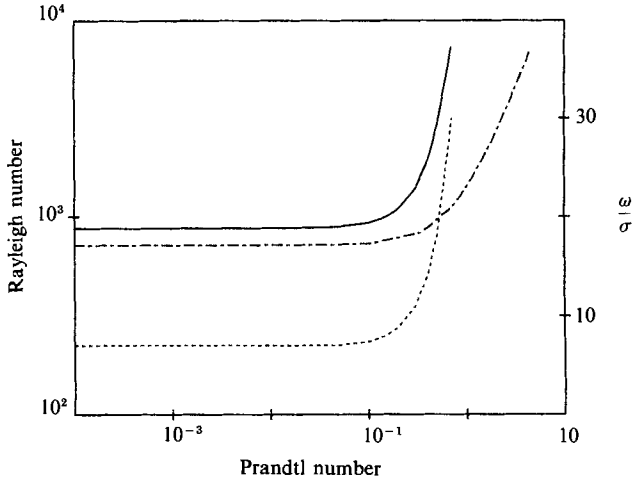

FIGURE 2. Rayleigh numbers R_T (dot-dashed line) and R_t (solid line) for the stationary and Hopf bifurcations described in the text, as a function of the Prandtl number for $a = 2.22$, $C = 1/\sqrt{6}$, together with ω/σ (dotted line), where ω is the angular frequency for the Hopf bifurcation. The asymptotic values for $\sigma \ll 1$ are $R_T = 720$, $R_t = 874.5$ and $\omega/\sigma = 7.02$.

4. Time-dependent solutions

The systems (2.2) and (3.1) with boundary conditions (2.3) have been time-marched for Rayleigh numbers larger than R_t, the Hopf bifurcation point (see the Appendix for details on the numerical schemes). As a default value $\sigma = 0.025$ will be taken, for this is the Prandtl number for mercury and it is a value occurring well into the asymptotic region, as can be seen from figure 2. However, in order to give some idea of the kinds of solution obtained, in figure 3 kinetic energy, E_k, has been plotted, see §4.1 below, scaled as $E_k C^2 \sigma^{-2}$, for the steady and time-dependent solutions of both systems, much as in figure 1, but now including solutions for several σ-values in the asymptotic region. The choice of E_k instead of $N-1$ has been dictated by the fact that the latter is meaningless in (3.1).

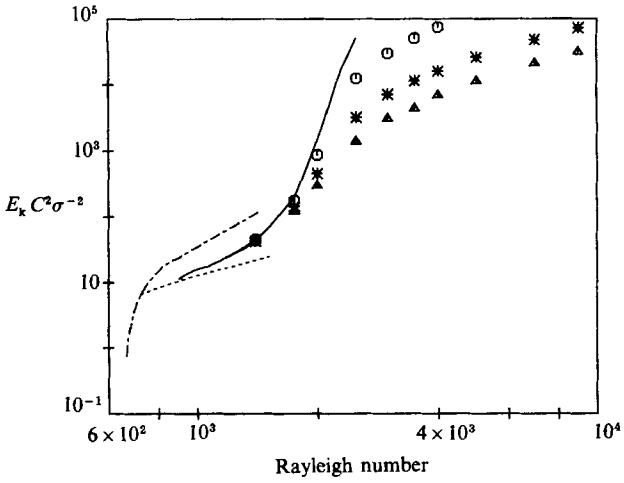

FIGURE 3. Kinetic energy, scaled as $E_k C^2\sigma^{-2}$, versus Rayleigh number for the steady solutions $\xi = 0$ (dot-dashed line) and $\xi \neq 0$ (dotted line) of (3.1), and the periodic solutions of both (3.1) (solid line) and (2.2), the latter for the values $\sigma = 0.01$ (⊙), $\sigma = 0.025$ (✳) and $\sigma = 0.04$ (△). In the range of values $R_t < R < 1300$ all time-dependent solutions merge.

In figure 3 we have plotted as a continuous line the time averages of E_k for the solutions of (3.1), and with circles, asterisks and triangles the solutions of (2.2) for $\sigma = 0.01$, 0.025, 0.04 respectively. We can identify two different sections plus a transition region. In the range of values $R_t < R < 1300$ all branches merge. It is in that region where figure 1 shows a plateau for $N-1$, with the fluxes being almost conductive, $N-1 = O(10^{-3})$. Solutions in that section display small Péclet numbers. For $R > 2500$ the kinetic energy, rather like the Nusselt number, becomes significantly larger as the Rayleigh number increases, although the curve for the Nusselt number flattens, with values going well below those for the $\xi = 0$ steady solutions. This is the intermediate Péclet-number regime.

Solutions of (3.1) have been found to be consistent with those of (2.2) for Rayleigh numbers in the small-Péclet-number regime, but outside that range differences increase very fast. To be precise, in that range shapes and periods for solutions of (2.2) and (3.1) are in perfect agreement if the corresponding Rayleigh numbers are shifted by a few percentage points, with the result that if solutions of both systems are plotted in figure 3 they become intermingled.

Outside the small-Péclet-number regime the approximation leading to (3.1) breaks down. There, and for small Prandtl numbers, $\tilde{W} \sim \sigma^{-n}$ and $\tilde{\theta} \sim \sigma^{-m}$ with n and m close to one – for a more precise discussion on n and m values, see below. It is worth mentioning here that Gough *et al.* (1975) and Toomre, Gough & Spiegel (1977) also showed the existence of two different asymptotic regimes, which they called the small and large $R\sigma$ limits, associated with small and large Péclet numbers although their results were for steady $\xi = 0$ solutions and the detailed phenomenology is different. Both regimes were also found in Paper I for rigid boundaries, as can be seen from figure 14 in that paper.

4.1. *Some relevant features of the time-dependent solutions*

As explained in §1, we have found a bifurcation to chaos induced by a symmetry invariance of the master system (2.2) and (2.3). There are in fact two such symmetries,

(i) skew-symmetry with respect to the midplane for $\{W, \theta, \bar{T}\}$:

$$\{+W(z,t), +\theta(z,t), +\bar{T}(z,t)\} \to \{-W(-z,t+t_0), -\theta(-z,t+t_0), -\bar{T}(-z,t+t_0)\},$$
$$+\xi(z,t) \to +\xi(-z,t+t_0),$$

(ii) symmetry with respect to reversals in ξ:

$$\{+W(z,t), +\theta(z,t), +\bar{T}(z,t)\} \to \{+W(z,t+t_0), +\theta(z,t+t_0), +\bar{T}(z,t+t_0)\},$$
$$+\xi(z,t) \to -\xi(z,t+t_0),$$

where t_0 is a time-lag constant. For fixed t_0 the previous set of symmetries replicates each solution four times. If there exists a replica identical to its original (i.e. the solution is invariant with respect to a symmetry) the solution will be said to be symmetrical. Also, for a periodic solution with $t_0 \neq 0$ we obtain $X(z,t+2t_0) = X(z,t)$ for every variable, with the result that the fundamental period is $t = 2t_0$, even if the period is $t = t_0$ for some variables. It will be shown below that these symmetric solutions grow from the reconnection of two $t = t_0$ asymmetric periodic solutions.

Small-Péclet-number regime

As a typical example of the small-Péclet-number regime we have chosen the solution obtained for $R = 10^3$, $\sigma = 0.025$. Its period in thermal unit times is $t = 64$, and the thermal flux is given by $N-1 = 1.6 \times 10^{-3}$ corresponding to an almost conductive regime. In order to describe its dynamics, in figure 4 are depicted the Reynolds number in the middle of the layer, the horizontally averaged helicity, the total kinetic energy E_k, together with the fraction of energy associated with the vertical vorticity E_ξ, and the phase ϕ, to be defined below. The energies have been defined as

$$E_k = \langle \tfrac{1}{2} v^2 \rangle = \int_{-\frac{1}{2}}^{+\frac{1}{2}} \tfrac{1}{2}\{a^{-2}[(\partial_z W)^2 + \xi^2] + W^2\}\, dz,$$

$$E_\xi = \int_{-\frac{1}{2}}^{+\frac{1}{2}} \tfrac{1}{2}\{a^{-2}\xi^2\}\, dz.$$

The value of the Péclet number, $Pe = \sigma Re$, for the periodic solution displayed in the figure, and for the maximum velocity amplitude during a cycle, is $Pe = 0.14$. The corresponding maximum Reynolds number is $Re = 5.7$. The reader will notice that both Re and Pe are measured using the same lengthscale, which need not be the only choice for a small-σ regime.

From the two upper curves in figure 4 we see that helicity keeps up with the Reynolds number though with a factor of ten difference in amplitude, in spite of the period for $\xi(0,t)$ being half that of $W(0,t)$, therefore reflecting the dominance of $\partial_z \xi(0,t)$ in $\bar{h}$ (see (2.6)). Concerning the energies, we can see in figure 4 the shift between the maxima of E_k and E_ξ, reflecting a periodic energy transfer from W to ξ, with the ratio q between both maxima taking the value $q = 0.356$.

Next, the phase-lag, $\phi(t)$, between $W(z,t)$ and $\theta(z,t)$ will be introduced:

$$\phi(t) = \frac{\int_{-\frac{1}{2}}^{+\frac{1}{2}} W\theta\, dz}{\left[\int_{-\frac{1}{2}}^{+\frac{1}{2}} W^2\, dz \int_{-\frac{1}{2}}^{+\frac{1}{2}} \theta^2\, dz\right]^{\frac{1}{2}}}.$$

For the solution displayed, the phase takes the value $\phi = 1$ throughout the entire

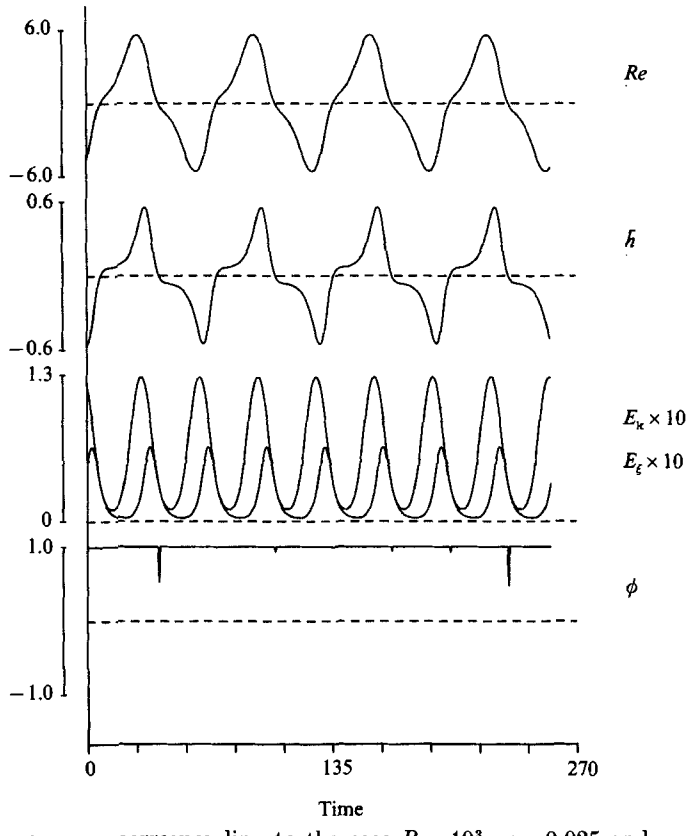

FIGURE 4. Time sequences corresponding to the case $R = 10^3$, $\sigma = 0.025$ and $a = 2.22$. The top curve shows the Reynolds number, $Re = CW/\sigma$, and below is the horizontally averaged helicity $\bar{h}$, both evaluated at $z = 0$. The following two curves display the total kinetic energy E_k together with the fraction of energy associated with the vertical vorticity E_ξ. The ratio $q = \langle E_k \rangle / \langle E_\xi \rangle$ is $q = 0.356$, and the period in thermal units is $t = 64$. The bottom figure shows the phase-lag ϕ – see the text.

period except, perhaps, during a very short time interval, with its value decreasing suddenly, then regaining its original value immediately, thus appearing as a very thin and short spike, possibly of numerical origin. Therefore, in the small-Péclet-number regime, velocity and temperature are coherent. This is a consequence of the fact than W and θ are linearly related by $\tilde{W} = -\nabla^2 \tilde{\theta}$ (see (3.1*c*)), together with an almost sinusoidal z-dependence.

Intermediate-Péclet-number regime

As a specific example of the intermediate-Péclet-number regime we have chosen the solution obtained for $R = 5 \times 10^3$, $\sigma = 0.025$. The maximum value for the Péclet number is now $Pe = 2.3$, which we take as an indication of an intermediate-Péclet-number regime. The maximum Reynolds number value is $Re = 92$, more than an order of magnitude larger than for the previous case, the thermal flux now being $N - 1 = 0.287$, with conduction still showing the largest contribution. The period in thermal unit times is $t = 0.46$, more than a hundred times smaller than the one shown previously.

As in the previous case, displayed in figure 5 are the Reynolds number, Re, measured at the centre of the layer, along with the averaged helicity, $\bar{h}$, and the total

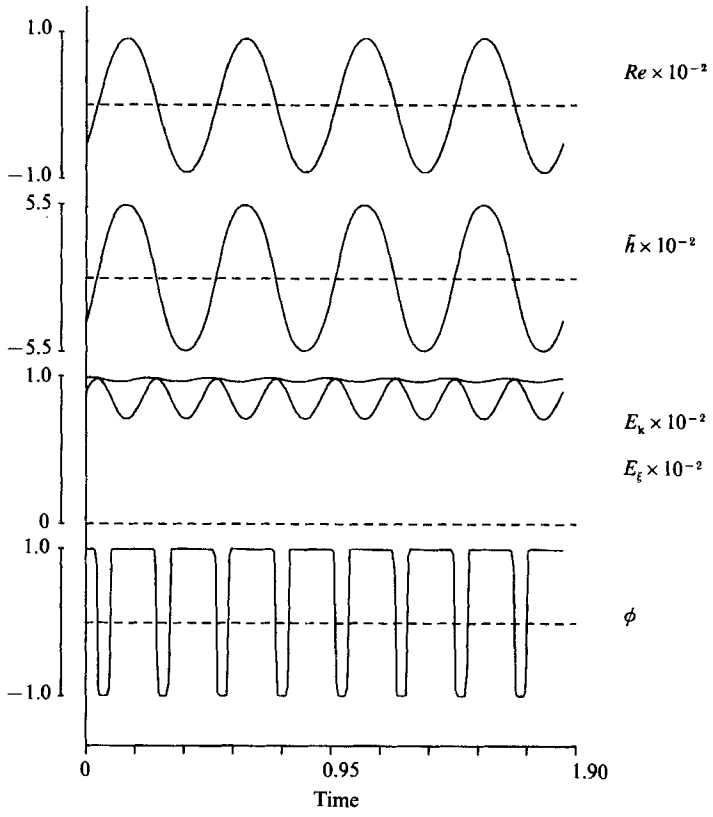

FIGURE 5. As figure 4, but for the case $R = 5 \times 10^3$, $\sigma = 0.025$ and $a = 2.22$. The ratio q is now $q = 0.86$ and the period is $t = 0.46$.

kinetic energy, E_k, together with the kinetic energy associated with the vertical vorticity E_ξ. Now the most relevant result is the large contribution of E_ξ to the total energy E_k, with the ratio between both maxima being $q = 0.86$, a very large fraction if we realize that most of the kinetic energy is stored permanently in the vertical vorticity field.

Also been displayed in figure 5 is the phase-lag $\phi(t)$, which looks like a comb, with ϕ jumping periodically from $\phi = +1$ to $\phi = -1$. For that solution the comb tooth thickness is, approximately, 25% of the whole period, giving an average value $\phi_{av} \sim 0.5$. The change in sign for ϕ at each cycle corresponds to a change in sign for the buoyancy work $\langle W\theta \rangle$, the brackets denoting spatial average. Therefore, that solution consists of a periodic sequence of buoyancy pushes and buoyancy brakes. In contrast to that, for the solutions of (3.1) $\langle W\theta \rangle = \langle |\nabla\theta|^2 \rangle$ is positively defined all along the cycle, as is $\phi(t)$. It is because of that absence of braking that amplitudes for the solutions of (3.1), as measured by the local Reynolds number $\tilde{W}$, grow much larger than the corresponding ones for (2.2).

In order to obtain more detailed information about phases and heat flux efficiency we have computed the exponents in $\tilde{W} \sim \sigma^{-n}$ and $\tilde{\theta} \sim \sigma^{-m}$. The precision obtained is not very satisfactory because of the high spatial resolution required, and also because the system goes to chaos through a quasi-periodic regime the description of which falls outside our scope. For the record, for $R = 10^4$ and $\sigma = 10^{-3}$, and from the steepness of the curve of maximum values of $\tilde{W}$ and $\tilde{\theta}$ against σ, the values $n = 0.86$

and $m = 0.94$ have been obtained, with both these figures still increasing slightly as σ decreases. For the time average of the Nusselt number the limit $N-1 \sim \sigma^{0.41}$ has been obtained, and from this limit the phase average ϕ_{av} can be estimated. By writing $N-1 \sim \phi_{\mathrm{av}} W\theta \sim \phi_{\mathrm{av}} \sigma^{2-n-m}$ we can estimate $\phi_{\mathrm{av}} \sim \sigma^{0.21}$, to be compared with the expression for the small-Péclet-number regime, where $n = m = 0$, $\phi_{\mathrm{av}} = 1$ (see figure 4) and, therefore, $N-1 \sim \sigma^2$.

4.2. *Qualitative description of a sequence to chaos*

In the small-Péclet-number regime we have found a cascade of bifurcations to chaos and subsequent relaminarization. Such a sequence has been described in the $\{W(0,t), \xi(0,t)\}$ phase-map projection with no reference to the variable $\theta(0,t)$ for, as is discussed above, θ and W are in phase. Figure 6 shows a sequence of solutions showing the most relevant steps in the hierarchy of bifurcations. Time dependence begins with a Hopf bifurcation and, as a consequence, W and ξ oscillate with the same period. If the Rayleigh number is increased the system goes through reconnection of an orbit with its symmetrical partner, to a symmetric orbit. This is clearly an homoclinic explosion with the saddle point located at the origin. Then the symmetry is broken and a pair of asymmetric solutions are formed, though only one is shown in the figure. This is a pitchfork bifurcation with the symmetric solution losing stability in favour of the two asymmetric ones. Later on, the asymmetric solutions reconnect again to build a new symmetric solution with its period doubled, and the process is repeated again and again until chaos is reached. If the Rayleigh number is increased beyond that chaotic region a relaminarization process occurs following a similar sequence of events but now working backwards. This scenario is similar to the one described by Kuramoto & Koga (1982) for the Ginzburg–Landau equation (see also Kuramoto 1984 for further discussion). Arneodo, Coullet & Tresser (1981) have also examined a modified Lorenz system displaying a similar scenario.

At first sight the cascading process described in figure 6 might seem to be one more example of a typical subharmonic period-doubling cascade (Feigenbaum 1978). But it is not. Most period-doubling cascades are induced by local instabilities. Orbits lose stability because the dominant Lyapounov multiplier goes through the value $\lambda = -1$, so they split up. If solutions are symmetric, period doubling requires, generically, a breaking of symmetry before the onset of the cascade (Swift & Wiesenfeld 1984). The main ingredients for the subharmonic cascade in figure 6 are totally different, as period doubling is associated with a homoclinic explosion, not with a continuous growing of the Lyapounov multipliers. Technically, a homoclinic explosion concerns the global structure of the flow, while classical period-doubling cascades involve only its local structure (see, for instance, Guckenheimer & Holmes 1983), so we shall call the present scenario a global subharmonic period-doubling cascade.

In order to analyse the cascade of subharmonic period doublings we present in figure 7 a sequence of Fourier spectra for $W(0,t)$ and $\xi(0,t)$ corresponding to $R =$ 1065, 1066, 1067. We have called a solution S_n or A_n^m depending on whether it is symmetrical or asymmetrical, with n or (n,m) meaning the number of loops in each upper quarter of the ξ *vs.* W phase-map projection. With that notation the sequences in figures 6 and 7 read, respectively, $A_1^0, S_1, A_1^1, S_2, A_2^2, S_4$, etc., and S_4, A_4^4, S_8.

First, we should notice that W doubles its period from A_n^n to S_{2n} while ξ does so from S_n to A_n^n and, also, that ξ-spectra display peaks for every integer multiple of the fundamental frequency, while W-spectra do so only for A_n^n, but not for S_n solutions, where only odd multiples of the fundamental frequency are present. Therefore, a

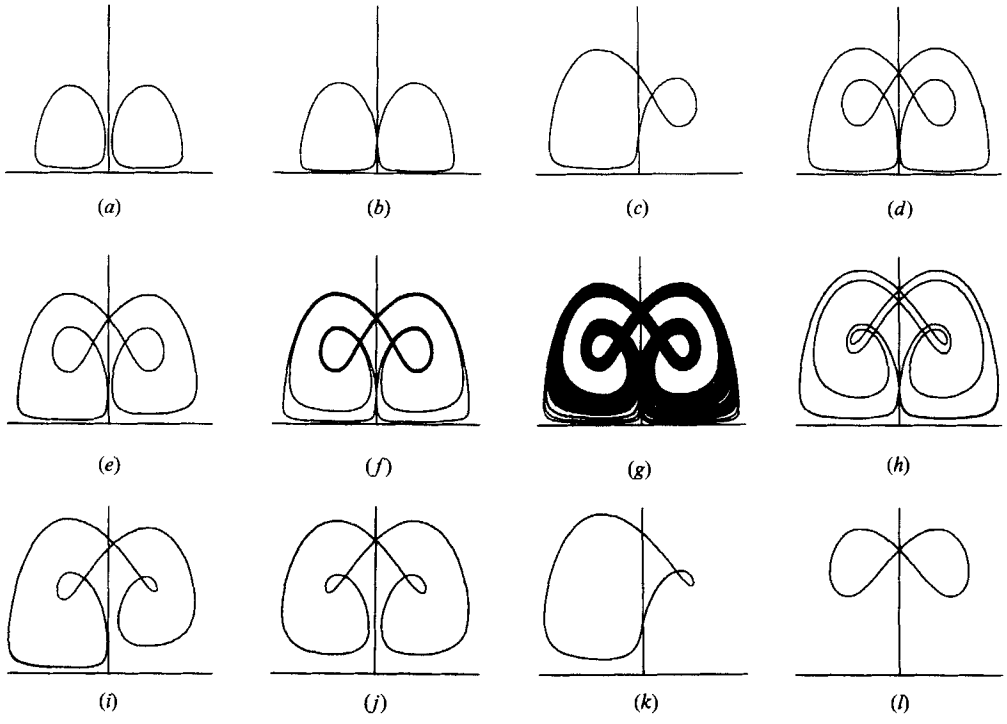

FIGURE 6. Phase-map projections for solutions of (2.2) with $\sigma = 0.025$ and $a = 2.22$. We have plotted $Re_v = C\xi/\sigma$ versus $Re = CW/\sigma$, both evaluated at $z = 0$. The minimum and maximum values in the plots are $0 < Re_v < 21$ and $-8 < Re < 8$ in every plot. Shown are: (*a*) $R = 930$ $[A_1^0]$, (*b*) $R = 940$ $[S_1]$, (*c*) $R = 1050$ $\{A_1^1]$, (*d*) $R = 1054$ $[S_2]$, (*e*) $R = 1061$ $[A_2^2]$, (*f*) $R = 1065$ $[S_4]$, (*g*) $R = 1100$ [chaos], (*h*) $R = 1145$ $[S_4]$, (*i*) $R = 1147$ $[A_2^2]$, (*j*) $R = 1155$ $[S_2]$, (*k*) $R = 1175$ $[A_1^1]$, (*l*) $R = 1300$ $[S_1]$.

sequence of ξ-spectra cannot be differentiated from a local subharmonic period-doubling cascade, while a sequence of W-spectra can. This is an important observation as, hitherto, most cascades have been identified from their Nusselt-number spectra, which are qualitatively similar to ξ-spectra, and not from their Reynolds-number spectra.

Finally, in order to differentiate both types of cascades, the Poincaré map for the chaotic solution $R = 1100$ is depicted in figure 8. We chose to plot values of W_{k+1} *vs.* W_k for $\xi = 14.3$. The non-local nature of the chaotic process can be seen from that plot. The steepness of the curve interpolating between the points of the Poincaré map being larger than one, any nth-order return map will be unstable everywhere. However, because of the symmetry of the return map, the representative point in phase space cannot escape. In contrast, most local period-doubling cascades are associated with quadratic return maps. A return map similar to the one shown in figure 8 has been discussed in detail by Sparrow (1982) and Guckenheimer & Holmes (1983) for the Lorenz attractor.

Description of a chaotic solution

As a typical example of chaotic solution we have taken $R = 1100$, $\sigma = 0.025$. Its phase and return maps have been included, respectively, in figures 6(*g*) and 8. In figure 9 we have plotted the time sequences for the Reynolds and Nusselt numbers

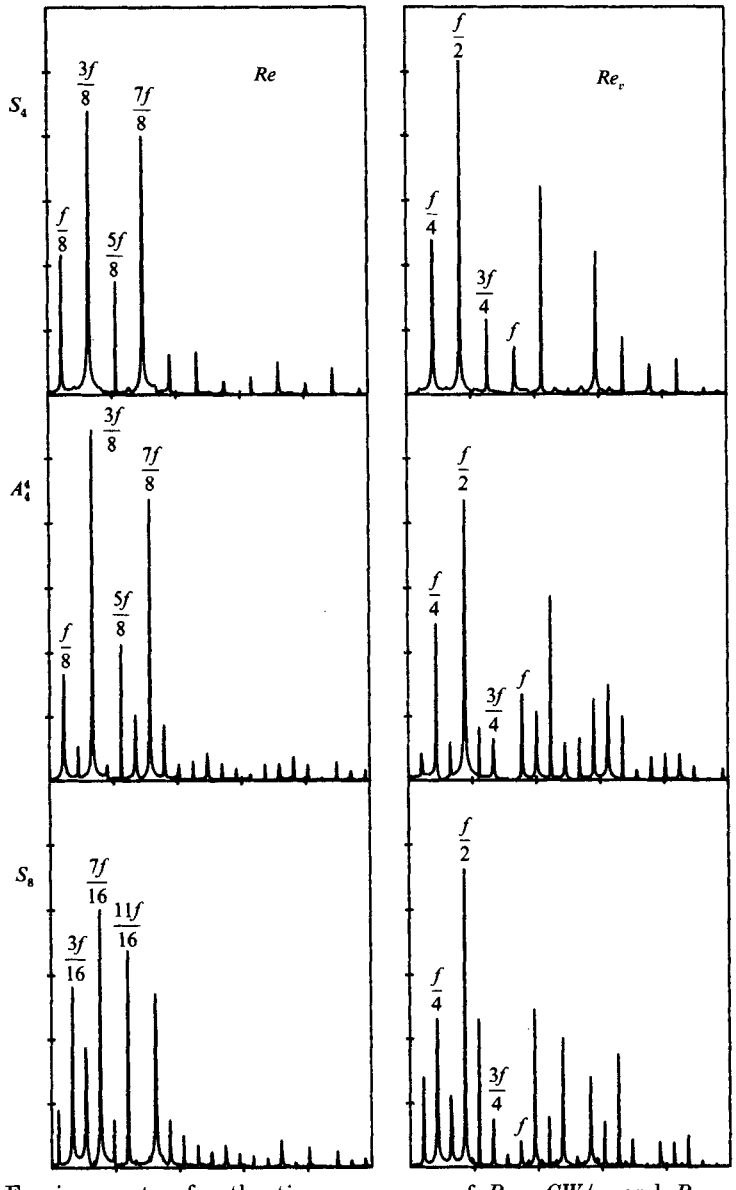

FIGURE 7. Fourier spectra for the time sequences of $Re = CW/\sigma$ and $Re_v = C\xi/\sigma$ at $z = 0$, corresponding to the Rayleigh-number values $R = 1065$ $[S_4]$, $R = 1066$ $[A_4^4]$ and $R = 1067$ $[S_8]$. Notice that Re doubles period from A_4^4 to S_8 while Re does so from S_4 to A_4^4. We have not displayed the Nusselt-number spectra because they are qualitatively similar to the Re_v spectra. To prevent scaling problems, we have not plotted the continuous component in the Re_v spectra. In the plot we have denoted the fundamental frequency by f, which corresponds, approximately, to the Hopf bifurcation frequency.

together with their Fourier spectra. It is a chaotic flow for it shows broad-bands, which is usually taken as an operational definition of stochastic or chaotic behaviour (Landford 1982). However, as mentioned by Landford, convective systems usually show, for the stochastic component, a small amplitude superimposed onto a much larger periodic component, and this is true for the Nusselt number but not for the Reynolds number.

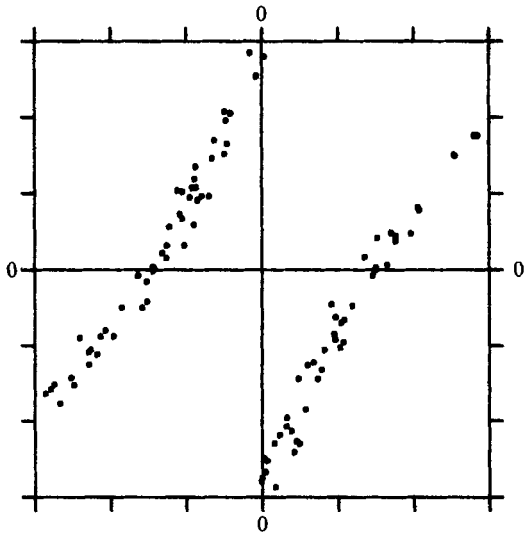

FIGURE 8. Poincaré return map Re_{k+1} *vs.* Re_k for the chaotic solution $R = 1100$, $\sigma = 0.025$ and $a = 2.22$. We have taken as a surface of section $Re_v = 14.3$ in the plot of figure 6(*g*).

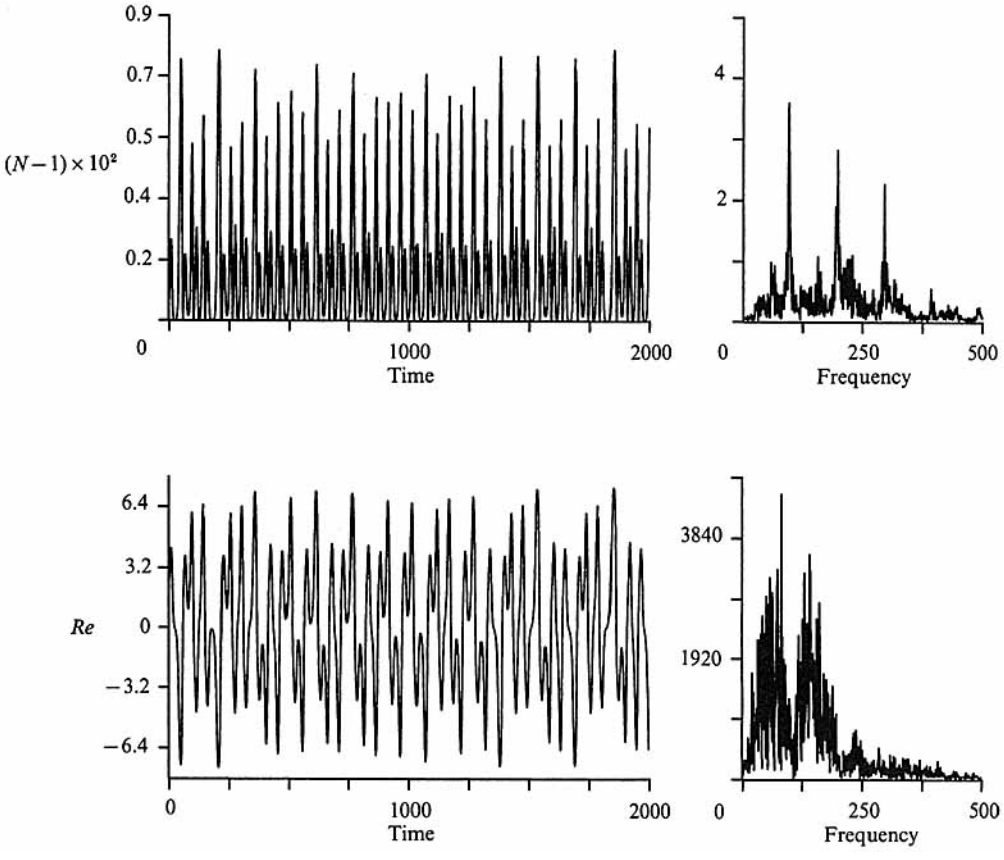

FIGURE 9. Time sequences for the Reynolds and Nusselt numbers, together with their Fourier spectra, for the chaotic solution $R = 1100$, $\sigma = 0.025$ and $a = 2.22$ (figure 6*g*). The unit for the frequency axis is $f = 1/5000$. The reader may notice a relative shift between the dominant peaks of both spectra.

The qualitative differences between the spectra of Re and N are even more substantial, as there is no clear relationship between their dominant frequencies (i.e. the peaks with larger amplitudes). This is not an accidental result but is a persistent feature of every chaotic solution computed. In our opinion such a difference results from the fact that both manifestations of chaos are accumulation points of two different sequences, as suggested by figure 7, with the Nusselt number behaving as ξ. The scenario for the Nusselt number looks like the one expected for a quadratic map while that for W does not. Therefore, depending on which variable is being measured, two different types of chaos can be observed: an almost periodic, poorly chaotic, thermal process, or a strongly chaotic hydrodynamical flow.

4.3. *On a low-order system*

In previous sections some indications have been found of a lack of z-structure in the small-Péclet-number regime, as can be seen, for instance, from the high degree of coherence between W and θ mentioned in §4.1. Therefore, to help in the diagnosis of the period-doubling cascade, a low-order system for (3.1) has been devised. The following truncation has been assumed:

$$W = \tfrac{3}{2}\pi(\pi^2+a^2)^{-1}(x_1 \sin \pi z + x_2 \sin 2\pi z),$$
$$\xi = \tfrac{3}{2}\pi(\pi^2+a^2)^{-\frac{3}{2}}(x_3 + x_4 \cos \pi z + x_5 \cos 2\pi z),$$

where, to make the expansion more obvious, we have shifted the origin for the z-coordinate to the bottom of the layer. Rescaling the time as $\tau' = (\pi^2+a^2)\tau$ and introducing the following definitions:

$$r = Ra^2/(\pi^2+a^2)^3 - 1, \quad s = q^3(r+1) - 1,$$
$$p = a^2/(\pi^2+a^2), \quad q = (\pi^2+a^2)/(4\pi^2+a^2)$$

the system (3.1) reduces to

$$\left.\begin{aligned}
\dot{x}_1 &= rx_1 + x_1 x_2 - x_4 x_5 - 2x_3 x_4,\\
\dot{x}_2 &= q^{-1}sx_2 - qx_1^2 - qx_4^2 - 4qx_3 x_5,\\
\dot{x}_3 &= -px_3 + \tfrac{2}{3}x_4 x_1 + \tfrac{4}{3}x_5 x_2,\\
\dot{x}_4 &= -x_4 + x_5 x_1 + x_4 x_2 + \tfrac{2}{3}x_3 x_1,\\
\dot{x}_5 &= -q^{-1}x_5 + \tfrac{4}{3}x_3 x_2.
\end{aligned}\right\} \tag{4.1}$$

In the present case $p = q = \frac{1}{3}$. The steady bifurcation to $\xi \neq 0$ takes place at $r = 0.1$, the Hopf bifurcation at $r = 0.33$ and chaos appears at $r = 0.59$.

If the plane x_1, x_3 is taken for the phase-map projection, a sequence is obtained that can hardly be differentiated from that displayed in figure 6. Taking the plane x_1, x_4 as a projection, the sequence is very similar to that obtained by Kuramoto & Koga (1982), Kuramoto (1984) for the Ginzburg–Landau equation. Such a coincidence might not be surprising, as all of them share the same type of symmetries. These symmetries are in the present case

$$\{+x_1, +x_2, +x_3, +x_4, +x_5\} \to \{-x_1, +x_2, +x_3, -x_4, +x_5\},$$
$$\{+x_1, +x_2, +x_3, +x_4, +x_5\} \to \{+x_1, +x_2, -x_3, -x_4, -x_5\},$$

with all the dynamics described before being associated with the first symmetry. However, by imposing $x_5 = 0$ we obtain a fourth-order system with the same set of

symmetries but showing only the head and tail of the period-doubling cascade, and certainly not chaos, suggesting that something other than symmetry is required for chaos.

System (4.1) has been used to explore the scenario in more detail and, in particular, to estimate the accumulation point μ_∞ for the period-doubling sequence, with μ_n defined as

$$\mu_n = \frac{r_{n+1} - r_n}{r_n - r_{n-1}},$$

where r_n is the bifurcation value for the solution S_N, and $N = 2^{n-1}$. We have obtained $\mu_4 = 0.354\ldots$, to be compared with the universal value for quadratic maps $\mu_\infty = 0.214\ldots$, showing that global cascades do not share in that universality.

4.4. *On the conservation of angular momentum*

The spontaneous growth of a vertical vorticity component can result in a sudden increase in the vertical component of the angular momentum of the flow even if, as assumed here, the spatial average of the vertical vorticity remains zero throughout the period. There is nothing against first principles in that result if at least one of the boundaries of the volume is not stress-free, but it certainly challenges intuition. The shape assumed in (2.1) could be questioned on that basis. For instance, if $f(x, y)$ is a hexagonal planform, the volume average of the vertical component L_z of the angular momentum is

$$\langle L_z \rangle = 6^{\frac{5}{2}} a^{-2} \pi \int_{-\frac{1}{2}}^{+\frac{1}{2}} \xi(z, t)\, \mathrm{d}z,$$

and taking for ξ a solution of (2.2) $\langle L_z \rangle \neq 0$.

It has been shown before that our master system is invariant with respect to vorticity reversals, $\xi \to -\xi$, but the corresponding solutions are time-lagged. In order to build a solution showing that symmetry throughout the time and, therefore, keeping a zero mean vertical angular momentum, $\langle L_z \rangle = 0$, the original expansion (2.1) must be extended. The most natural way to do so is to take a system made up of two hexagonal planforms, one up and one down. It will be shown below how that system displays most of the one-mode dynamics.

Let (2.1) be changed to

$$v_z = \sum f_i(x, y)\, W_i(z, t),$$

$$\omega_z = \sum f_i(x, y)\, \xi_i(z, t),$$

$$T = \bar{T}(z, t) + \sum f_i(x, y)\, \theta_i(z, t) \quad (i = 1, 2),$$

where $f_1(x, y)$ is an hexagonal planform, $f_2(x, y) = -f_1(x + x_0, -y - y_0)$ and $f_1(x_0, y_0) = 0$. Under such conditions the equations to be solved are readily established. Equations (2.2*a–c*) are duplicated for the second mode, with $C_2 = -C$, whereas (2.2*d*) includes contributions from both modes. Therefore both modes interact only through the mean temperature field $\bar{T}$.

In the small-Péclet-number regime, $\partial_z \bar{T} = -1$ and both modes uncouple, so each one behaves as in the one-hexagon case. If the initial conditions are properly set, then $X_1(z, t) = X_2(-z, t)$ for each of the variables W, θ and ξ. As a consequence $\langle L_z \rangle = 0$ at any later time. In the intermediate-Péclet-number regime such a spatially symmetric solution still exists, though it need not be unique and could well be unstable. We have compared several such solutions and their dynamics is roughly similar to that described in this paper. The only difference to be reported is a factor

of two in the value of $N-1$, otherwise a small quantity. Thus it can be concluded that the whole dynamics need not be dependent on the conservation of the vertical component of the angular momentum.

5. Conclusions

In the present paper we have examined the dynamics of the vertical vorticity field in the framework of a highly truncated model of thermal convection. The model is intended for situations where straight rolls are not the dominant structures and, in particular, for low-Prandtl-number flows, where stable rolls might not even exist.

Truncated models can be suspected of being mathematical artifacts showing completely non-physical dynamics. This could certainly be the case for the present model. But as bifurcation points and timescales have been found in Paper I to be in reasonable agreement with experiments, we believe the system describes a real process, at least in the neighbourhood of this bifurcation, as suggested by the normal form theorem. It is on that region, i.e. in the low-Péclet-number regime, that we have concentrated our efforts and where the most exciting dynamics has been found.

One of the most striking results is the existence of a regular zero-Prandtl-number limit for mildly supercritical regimes. In that limit, advected heat is negligible, so it has been termed the small-Péclet-number regime, but the hydrodynamical activity is still large, as can be seen from the Reynolds number. In that regime chaos has been found, with the whole scenario being induced by a sequence of reconnections and symmetry breakings. It is a cascade of subharmonic period-doublings, but the whole scenario is different from the one expected for quadratic maps. In order to develop a deeper understanding of the model, a fifth-order system displaying exactly the same route to chaos has been derived.

Beyond the small-Péclet-number regime there is a family of solutions somewhat more efficient in advecting heat and showing larger Reynolds numbers. Their distinguishing feature is the reduced coherence between temperature and velocity. In contrast to the previously quoted solutions, the buoyancy work pushes and brakes the motion in every cycle to compensate for the reduced viscous damping. It is that reduced damping that might explain the large fraction of kinetic energy stored in the horizontal motion, in the vertical vorticity field, to be precise. A fraction that reaches values of 80% or 90% of the total kinetic energy. Such a large anisotropy is hard to believe, although it may be taken as a warning against some parameterization procedures. But truncation can be blamed for this unphysical behaviour, as it breaks the cascade towards the small scales and shortcuts the coupling between vertical vorticity and buoyancy.

The present work has been supported by the Direccion General de Investigacion Cientifica y Tecnica (DGICYT) under grants 1169/84 and PS87-0107.

Appendix. The numerical scheme

The system to be integrated shows a complicated bifurcation pattern that goes through a chaotic region. In addition, the system is stiff, with timescales being in a ratio of order 10^{-2} or even smaller. With such constraints three different schemes have been tested, all implicit in time. The numerical error has been estimated by comparing the periods and orbital shapes of periodic solutions obtained from two or three of these different methods. In each of the three methods the error has been

reduced as much as necessary, though the price paid in terms of CPU time and storage requirements has sometimes been very high. The error in the periods of periodic orbits has been taken as a test of the accuracy of a given method, because we know from the Floquet theory that any stable periodic solution is marginally stable in the direction tangent to its orbit in phase space. Therefore for periodic solutions the greatest sensitivity to error must be expected in that direction.

The first technique that we used was the implicit finite-differences scheme centred in space and advanced in time that was described in Paper I. It has been found accurate and stable but very slow, so it has only been used as a test. As a second technique a method of lines has been chosen where the space derivatives have been written in terms of centred finite differences (Walter 1970). The resulting system of ordinary differential equations can be written formally as

$$\dot{X}_j = A_{jkl} X_k X_l + B_{jk} X_k \quad (j,k,l = 1,n) \tag{A 1}$$

where $\{X_1, \ldots, X_n\}$, with $n = 4N$, are the values taken by the variables W, ξ, θ, and $\bar{T}$ at the N spatial mesh points and a dot means a time derivative. The system (A 1) has been solved using a Gear method, since it is implicit and particularly well suited for stiff systems (Gear 1971). The number N of mesh points for the space coordinate ranged between 70 and 100. The method has been found stable, accurate and much faster than the first one. However, CPU time increases substantially with increasing accuracy.

The third method tried, and the fastest one, was a Galerkin expansion for the z-coordinate in terms of trigonometric functions. The system of differential equations obtained can be written as (A 1), but now $\{X_1, \ldots, X_n\}$ are the $n = 4N+1$ amplitudes of the Fourier series for the variables W, ξ, θ, and $\bar{T}$. Now, as in the previous technique, the resulting time-dependent system of ordinary differential equations has been solved using a Gear method and for $N = 4$–24. This method has been found to be faster than the previous one. CPU time for a smooth, well-behaved periodic solution has been reduced by a factor of fifty with respect to the method of lines.

REFERENCES

Arneodo, A., Coullet, P. & Tresser, C. 1981 *Phys. Lett.* A **81**, 197.

Bolton, E. W. & Busse, F. H. 1985 *J. Fluid Mech.* **150**, 487.

Brandt, P. N., Scharmer, G. B., Ferguson, S., Shine, R. A., Tarbell, T. D. & Title, A. M. 1988 *Nature* **335**, 238.

Busse, F. H. & Bolton, E. W. 1984 *J. Fluid Mech.* **146**, 115.

Eckmann, J. P. 1981 *Rev. Mod. Phys.* **53**, 643.

Feigenbaum, M. 1978 *J. Statist. Phys.* **19**, 25.

Gear, C. W. 1971 *Numerical Initial Value Problems in Ordinary Differential Equations*, p. 209. Prentice Hall.

Gough, D. O., Spiegel, E. A. & Toomre, J. 1975 *J. Fluid Mech.* **68**, 695.

Graham, E. 1977 In *Problems of Stellar Convection* (ed. E. A. Spiegel & J. P. Zahn). Lecture Notes in Physics, vol. 41, p. 151. Springer.

Guckenheimer, J. & Holmes, P. 1983 *Nonlinear Oscillations, Dynamical Systems and Bifurcations of Vector Fields*. Springer.

Haken, H. 1983 *Synergetics*. Springer.

Jones, C. A., Moore, D. R. & Weiss, N. O. 1976 *J. Fluid Mech.* **73**, 353.

Knobloch, E., Moore, D. R., Toomre, J. & Weiss, N. O. 1986 *J. Fluid Mech.* **166**, 409.

Kuramoto, Y. 1984 *Chemical Oscillations, Waves and Turbulence*, pp. 132–137. Springer.

Kuramoto, Y. & Koga, M. 1982 *Phys. Lett.* A **92**, 1.

LANDFORD, O. E. 1982 *Ann. Rev. Fluid Mech.* **14**, 347.

MASSAGUER, J. M. & MERCADER, I. 1984 In *Cellular Structures in Instabilities* (ed. J. E. Wesfreid & S. Zaleski). Lecture Notes in Physics, vol. 210, pp. 270–277. Springer.

MASSAGUER, J. M. & MERCADER, I. 1988 *J. Fluid Mech.* **189**, 367 (referred to as Paper I).

NEWELL, A. C. & WHITEHEAD, J. A. 1969 *J. Fluid Mech.* **38**, 279.

SIGGIA, E. D. & ZIPPELIUS, A. 1983 *Phys. Fluids* **26**, 2905.

SPARROW, C. T. 1982 *The Lorenz Equations: Bifurcations, Chaos and Strange Attractors.* Springer.

SWIFT, J. W. & WIESENFELD, K. 1984 *Phys. Rev. Lett.* **52**, 705.

TOOMRE, J. 1988 *Nature* **335**, 202.

TOOMRE, J., GOUGH, D. O. & SPIEGEL, E. A. 1977 *J. Fluid Mech.* **79**, 1.

WALTER, W. 1970 *Differential and Integral Inequalities*, p. 275. Springer.

ZIPPELIUS, A. & SIGGIA, E. D. 1982 *Phys. Rev.* A **26**, 178.